SYMPOSIUM

Go Reconfigure: How Fish Change Shape as They Swim and Evolve

John H. Long, Jr,[1,]* Marianne E. Porter,* Robert G. Root[†] and Chun Wai Liew[‡]

*Department of Biology and Program in Cognitive Science, Vassar College, Poughkeepsie, NY 12604, USA;
[†]Department of Mathematics, Lafayette College, Easton, PA 18042, USA; [‡]Department of Computer Science,
Lafayette College, Easton, PA 18042, USA

[1]E-mail: jolong@vassar.edu

Synopsis The bodies of fish change shape over propulsive, behavioral, developmental, and evolutionary time scales, a general phenomenon that we call "reconfiguration". Undulatory, postural, and form-reconfiguration can be distinguished, studied independently, and examined in terms of mechanical interactions and evolutionary importance. Using a combination of live, swimming fishes and digital robotic fish that are autonomous and self-propelled, we examined the functional relation between undulatory and postural reconfiguration in forward swimming, backward swimming, and yaw turning. To probe how postural and form reconfiguration interact, the yaw turning of leopard sharks was examined using morphometric and kinematic analyses. To test how undulatory reconfiguration might evolve, the digital robotic fish were subjected to selection for enhanced performance in a simulated ecology in which each individual had to detect and move towards a food source. In addition to the general issue of reconfiguration, these investigations are united by the fact that the dynamics of undulatory and postural reconfigurations are predicted to be determined, in part, by the structural stiffness of the fish's body. Our method defines undulatory reconfiguration as the combined, point-by-point periodic motion of the body, leaving postural reconfiguration as the combined deviations from undulatory reconfiguration. While undulatory reconfiguration appears to be the sole or primary propulsive driver, postural reconfiguration may contribute to propulsion in hagfish and it is correlated with differences in forward, and backward, swimming in lamprey. Form reconfigures over developmental time in leopard sharks in a manner that is consistent with an allometric scaling theory in which structural stiffness of the body is held constant. However, correlation of a form proxy for structural stiffness of the body suggests that body stiffness may scale in order to limit maximum postural reconfiguration during routine yaw turns. When structural stiffness and undulatory frequency are modeled as determining the tail's undulatory wave speed, both factors evolve under selection for enhanced foraging behavior in the digital fish-like robots. The methods used in making these distinctions between kinds of reconfiguration have broad applicability in fish biology, especially for quantifying complex motor behaviors in the wild and for simulating selection on behavior that leads to directional evolution of functional phenotypes.

Introduction

The locomotion, behavior, development, and evolution of fish all require changes in body shape. Change in body shape, however it occurs, is a phenomenon that we call reconfiguration. Reconfiguration can occur simultaneously on three levels (Fig. 1): (1) undulatory reconfiguration, the ever-changing periodically repeating changes in body shape, usually but not always propulsive, overlaid on top of reconfiguration of form and posture (Root et al. 2007); (2) postural reconfiguration, transient, secular change in shape that can be momentary, such as bending the body during a turn, or, maintained, such as altering midline curvature at different, steady swimming speeds (Long 1995; Long et al. 2002; Porter et al. 2009); and (3) form reconfiguration, the static external and internal shape of the fish as if it were holding its body straight and not

undulating body or fins; this is the "neutral" anatomical reference position for fish and it changes during development and evolution. Using this conceptual framework, our goal is to understand how undulatory, postural, and form reconfiguration interact mechanically during locomotion and evolution.

Undulatory reconfiguration

To quantify undulatory reconfiguration, we take the axial and lateral motion of each mid-line point of a swimming fish and decompose the motion in each dimension into its periodic and secular components (Root et al. 2007). We created a method of harmonic decomposition that allows us to define the undulatory reconfiguration of any part of the body or the body itself as the fraction of the total axial and lateral motion of any point that can be explained by a fundamental sinusoidal frequency and its harmonics
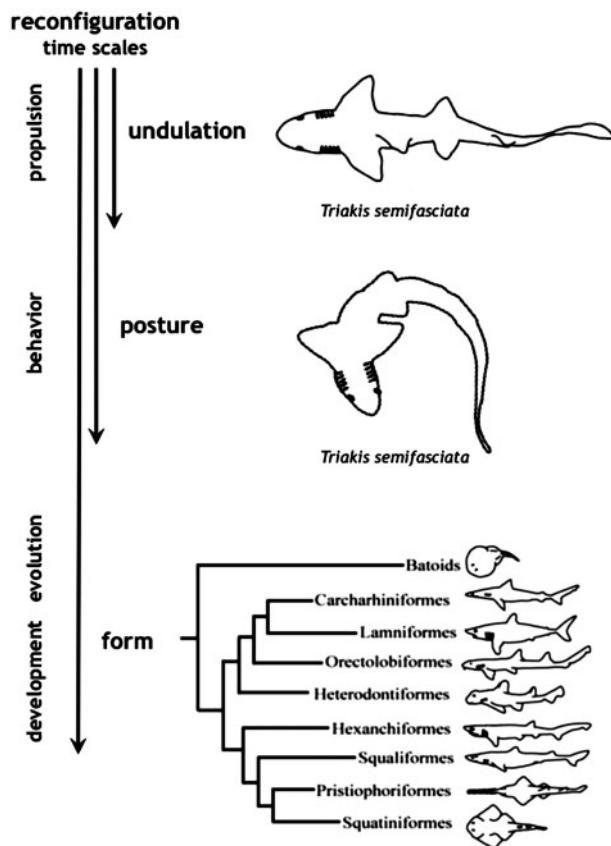

Fig. 1 Reconfiguration is change in body shape of three different kinds operating on three different time scales. Undulatory reconfiguration is the periodic point-by-point motion of the body or fins during propulsion. Postural reconfiguration is transient, as seen during yaw turning, and is involved with maneuvering behaviors. Form reconfiguration is change in the size and anatomical shape of the animal, includes both internal and external features, and changes over developmental and evolutionary time.

(Root et al. 2007). The periodic components are represented by Fourier series (Root et al. 1999). The secular components are (1) point-by-point velocities that deviate from that of the whole-body and (2) independent accelerations of the points. Our use of the term "secular" is meant to indicate the components that are spatially small and temporally large compared to the motion and time, respectively, of the undulatory cycle.

By this approach, the combined-harmonic motion of all the points on the body is, by definition, pure undulatory reconfiguration. To date, we have evidence that pure undulatory reconfiguration—reconfiguration without any secular components—is never seen in marine lamprey, *Petromyzon marinus*, swimming forward or backward (Root et al. 2007). We quantified the lampreys' variable deviation from pure undulatory configuration using what we called the unsteadiness index, here renamed the "postural reconfiguration index," P_r (see Equation [7]), in order to indicate that we can separately measure undulatory and postural reconfigurations.

Postural reconfiguration

Postural reconfiguration is measured as the deviation of body motion from pure undulatory reconfiguration in any situation. At one extreme, a routine yaw turn (Porter et al. 2009) or stage 1 of a fast-start escape (Hale et al. 2002) involve pure postural reconfigurations (Fig. 1). Given that the neuromuscular activation patterns underlying stage 1 escape behaviors are well established (Eaton et al. 2001), and differ from undulatory patterns (Jayne and Lauder, 1993), we predict that undulatory and postural reconfiguration are discrete physiological systems. At the same time, comparison of lamprey swimming forward and backward (Root et al. 1999, 2007) clearly show that undulatory and postural reconfiguration can be superimposed and that their relative contributions to body motion varied. What is unknown is how undulatory and postural-reconfiguration interact to control swimming performance.

Since swimming with large amounts of postural reconfiguration involves increased curvature of the body axis, we predicted that lamprey (Root et al. 1999), and perhaps other fishes (Long and Nipper 1996; Long et al. 2002a), actively control the structural stiffness, k_b $(N\,m^{-1})$, of their bodies. To date, evidence for active control of body curvature has been indirect, with whole-body work loops on bass, *Micropterus salmoides* (Long and Nipper 1996), and eel, *Anguilla rostrata* (Long 1998), showing the

capacity for control of stiffness, and with measurements of intramuscular pressure, coupled with electromyography, showing possible elastic storage of energy within skeletal structures in bichir, *Polypterus palmas* (Westneat et al. 1998).

Evidence for passive (i.e., non-muscular) variation in body stiffness influencing undulatory and postural reconfiguration comes from the skin-altered body stiffness of swimming longnose gar, *Lepisosteus osseus* (Long et al. 1996), the frequency-dependent mechanical properties of the bodies of Atlantic hagfish, *Myxine glutinosa* (Long et al. 2002b), correlations of stiffness morphometrics with body curvature of sharks during yaw turns (Porter et al. 2009), and the stiffness-altered changes in swimming performance in self-propelled fish-like models (McHenry et al. 1995) and fish-like robots (Long et al. 2006).

Form reconfiguration

If structural stiffness, k_b, of the body influences undulatory and postural reconfiguration, then we would expect the form of fish, over developmental time, to reconfigure accordingly. One hypothesis-driven way to measure form reconfiguration is by reference to scaling models, with isometric scaling as the null hypothesis. Using the stiffness framework, one alternative hypothesis is that allometric scaling controlled by k_b governs the form reconfiguration. As a crude first approximation of what is undeniably a complex mechanical situation, a fish's body can be modeled as a cantilevered beam:

$$k_b = \frac{E_b I_b}{L_b^3} \qquad (1)$$

where E_b is the body's apparent Young's modulus (Pa), I_b is the body's second moment of area (m^4), and L_b is the body's total length (m). We acknowledge the complexities of knowing E_b in a muscularly activated system interacting with an external fluid; our point here is to focus on and isolate the elastic properties of fish, properties that are often ignored in models of locomotion. With that in mind, we further simplify the model by assuming that E_b is constant, leaving the following proportionality, k', that we call the structural stiffness proxy:

$$k' \propto \frac{I_b}{L_b^3}. \qquad (2)$$

This proportionality leads to the prediction that if k_b remains constant as form reconfigures over developmental time, I_b should scale allometrically as follows:

$$I_b \propto \left(L_b^3\right)^1 \qquad (3)$$

compared to isometric scaling (note that I_b is in units of m^4 and L_b^3 is in m^3):

$$I_b \propto \left(L_b^3\right)^{\frac{4}{3}}. \qquad (4)$$

Alternatively, form reconfiguration may scale in a way that conforms neither to simple isometric nor to allometric scaling models. For example, k_b may vary with form reconfiguration to control postural reconfiguration. To limit postural reconfiguration during yaw turns, larger bodies may increase k_b and compensate for increased inertial forces with increasing body mass. If form reconfiguration is related to k_b in this manner, we would expect that variation in k' would correlate inversely with the magnitude of postural reconfiguration during behaviors such as routine yaw turning. Postural reconfiguration during yaw turns is measured by the body-bending coefficient, B_b, a dimensionless number:

$$B_b = 1 - \frac{L_l}{L_b} \qquad (5)$$

where L_l is the chord length from the tip of the rostrum to the tip of the tail at rotation of the head through $90°$ during a yaw turn (Porter et al. 2009).

Evolution of undulatory and postural reconfiguration

While we presented the view that undulatory and postural reconfiguration occur in propulsive and behavioral time (Fig. 1), the mechanical and physiological underpinnings that control these types of reconfiguration, such as the structural stiffness of the tail, k_t, and the frequency of the undulatory cycle, f, may be subject to changes over both developmental and evolutionary time scales, as discussed for k_b in the previous section. Given the likely role of k_t in both undulatory and postural reconfiguration, we would predict that selection on behaviors that involve swimming and maneuvering would influence the evolution of the k_t of a population. Furthermore, since f is under neural control and determines the rate of undulatory reconfiguration, we consider that it, too, may evolve when selection acts on behavior.

Using embodied, autonomous, and self-propelled fish-like robots called Tadros, we tested the hypothesis that k_t and undulatory reconfiguration evolve under selection for enhanced forage navigation (Long et al. 2006). We use the term "forage navigation" to describe any behavior in which an individual detects an environmental gradient, such as light or an odorant, and uses that gradient to navigate to a food source. A small population ($n = 3$) of

Tadros with biomimetic tails of variable k_t showed, over 10 generations, a strong positive relationship between increases in k_t and improved forage navigation. Furthermore, increasing k_t increased the lateral motion of the tail, an evolutionary change in undulatory reconfiguration. When we doubled the population size ($n = 6$), added a predator robot, and included a neural escape mechanism to help the Tadros avoid the predator, k_t increased under selection for enhanced predator avoidance and forage navigation (Doorly et al. 2009). However, in spite of these interesting findings, the evolution of embodied robots is severely limited by the number of person-hours required to build new robots and conduct trials. To permit larger population sizes, more generations, and more evolutionary scenarios, we present an alternative to physically embodied robots: digital Tadros, self-propelled, and autonomous, in an evolutionary simulation. We allow k_t and f of the digital Tadros to vary independently in two different evolutionary worlds and to co-vary in another.

Go reconfigure

The reconfiguration framework outlined above delineates undulatory, postural, and form reconfiguration. These three kinds of reconfiguration are necessary and sufficient to measure how the shape of a fish changes over locomotor, behavioral, developmental, and evolutionary time. For any specific system, information about the three kinds of reconfiguration must be compiled and integrated, preferably while testing hypotheses. What we offer here are three examples of how to explicitly test hypotheses related to the different kinds of reconfiguration. We also attempt to integrate the different kinds of information about reconfiguration by focusing on structural stiffness of the body. We conducted three different analyses that partially span the time scales of reconfiguration. First, we analyzed the volitional translational swimming of Atlantic hagfish, *M. glutinosa*, and marine lamprey, *P. marinus*, in order to quantify and delineate undulatory and postural reconfiguration. Next, we examined routine yaw turns of the leopard shark, *Triakis semifasciata*, in order to examine postural reconfiguration in the context of form reconfiguration during development. Lastly, we simulated the evolution of forage navigation behavior of fish-like digital Tadros in order to determine how reconfiguration mechanisms might change under selection pressure.

Methods

Undulatory and postural reconfiguration

Seven parasitic-phase, metamorphosed marine lamprey, *P. marinus*, with total body lengths, L_b, between 10 and 17 cm, were videotaped at 500 images per second (Kodak Ektapro model 1000 EM) as they swam forward and backward in a still-water tank. To prevent optical distortions caused by surface waves in the tank, their ventral surfaces were recorded through a glass bottom (for more details, see Root et al. 2007). In the same manner, eight Atlantic hagfish, *M. glutinosa*, with L_b between 28 and 33 cm, were videotaped at 60 images per second (Hitachi model KP-M1U) as they swam forward in a still-water circuit (for more details, see Long et al. 2002). Video sequences were manually digitized, with 20 points evenly spaced along the axial midline. The on-screen cursor was used to gauge the mid-point between lateral edges of the body in ventral view. Using a custom spline routine developed by Jayne and Lauder (1993), we reconstructed the midline of both lamprey and hagfish to have a total of 31 points.

For any point on the body, i, deviations from undulatory configuration can be measured as the difference in that point's velocity vector, v_i, and the average velocity vector of all the points on the body, $\bar{v}$, scaled by the composite speed of the whole body, $|\bar{v}|$. We call this scaled vector the undulation error, $\vec{U}_{e_i}$:

$$\vec{U}_{e_i} = \frac{v_i - \bar{v}}{|\bar{v}|} \qquad (6)$$

Note that $|\bar{v}|$ is the average scalar of all the v_i over the entire analysis sequence; it represents an important departure from standard measurements of swimming speed, taken from a single reference point such as the tip of the rostrum, and will be used throughout this study.

When the $\vec{U}_{e_i}$ are plotted for each point, as we move the one-cycle analysis window through the locomotor sequence of interest, in some cases the $\vec{U}_{e_i}$ are extremely small, indicating nearly pure undulatory reconfiguration, and in some cases the cloud of $\vec{U}_{e_i}$ are large, indicating superimposition of undulatory and postural reconfigurations (Fig. 2A and B). Thus the $\vec{U}_{e_i}$ from all body points, 0 to 30, are used to calculate the postural reconfiguration index, P_r:

$$P_r = \sqrt{\frac{\sum_{i=0}^{i=30}\left[\left(\left|\vec{U}_{e_i}\right|\right)^2\left(\frac{\bar{v}}{|v_i|}\right)\right]}{n-1}}, \qquad (7)$$

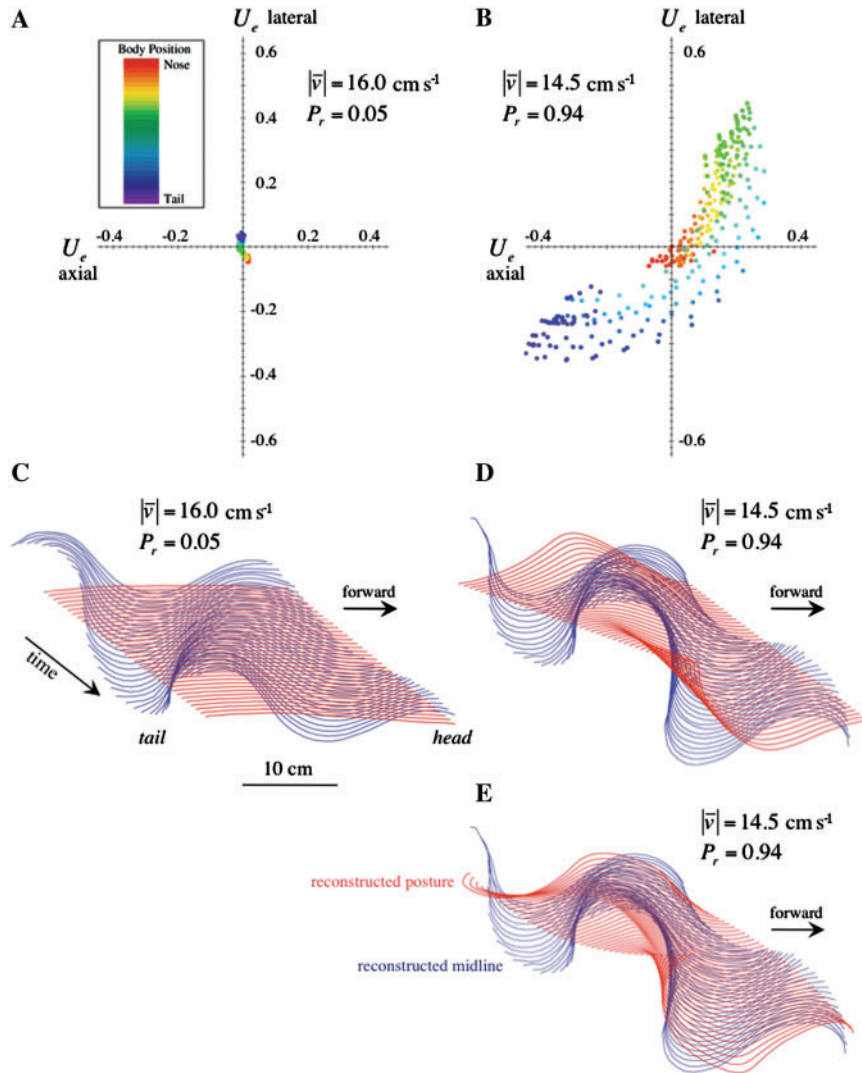where n is the number of full-cycle analysis windows.

Fig. 2 Undulation errors and postural reconfiguration index. (A) Small-magnitude undulation errors, $\vec{U}_e$, lead to a small postural reconfiguration index, P_r. This hagfish is swimming in a nearly perfect undulatory mode, with most reconfiguration due to undulation. (B) Large-magnitude $\vec{U}_e$ lead to a large P_r. Same hagfish as in A. Even though whole-body composite speeds, $|\bar{v}|$, are similar, the $\vec{U}_e$ are not. In this instance, the tail (blue points) has negative axial and lateral speed compared to the $|\bar{v}|$. The rostral points (orange points) show little deviation from the $|\bar{v}|$. Mid-body points (green) show the opposite trend seen in the tail points. (C) Reconstructed midline (blue) and posture (red) for the trial shown in (A). The midline is reconstructed from the fundamental frequency, f_0, its first harmonic, f_1, and a secular velocity, $\dot{u}$ for each point in the axial and lateral dimension (Fig. 3); a secular acceleration term, $\ddot{u}$, is added for (E). The non-harmonic components of the motion yield the postural midline (in red). (D) Large-magnitude P_r, as shown by the standing wave of the change in the postural midline. (E) Second-order term added to improve fit (Fig. 3). Note change in amount of curvature on the posture midline.

We calculate a second postural reconfiguration metric, the summary postural curvature, $\bar{\kappa}_p$, which measures the average curvature of the body that is not caused by undulatory reconfiguration. We first fit the motion of each body point, i, in axial, u, and lateral, v, dimensions to a function of the form (here shown for the axial dimension, u):

$$u_i = u_0 + \dot{u}t + \frac{\ddot{u}}{2}t^2 + a_f \cos(\omega t - \phi_f)$$
$$+ a_1 \cos(2\omega t - \phi_1) \tag{8}$$

where u_0 is the point's starting postural position, $\dot{u}$ is the point's secular velocity, $\ddot{u}$ is the point's secular acceleration, a_f and a_1 are the amplitudes of the fundamental and first harmonic frequencies, respectively, ω is the fundamental angular frequency, and ϕ_f and ϕ_1 are the phase lags for the fundamental and first harmonic frequencies, respectively (for full methodology see Root et al. 2007). Pure undulatory reconfiguration occurs when $\dot{u}$ and $\ddot{u}$ are zero. In most cases, however, applying multiple-linear regression to determine these quantities from actual

data, the non-periodic components of Equation (8) are significantly different from zero.

We next calculate a posture midline through time, the position of the body less its undulatory motion, which allows us to visualize the postural reconfiguration (red lines in Fig. 2C–E). To create these postural midlines, we use the linear functions (Equation [8]) to generate a series of u_{ij}, v_{ij} data points for each body point, i, and each video frame, j. Curvature of the postural midline at any point and time, κ_{ij}, is estimated using centered-difference approximations, which yield:

$$\kappa_{ij} = 8 \frac{\begin{array}{c}(v_{(i+1)j} - v_{(i-1)j})u_{ij} - (u_{(i+1)j} - u_{(i-1)j})v_{ij} \\ + u_{(i+1)j}v_{(i-1)j} - u_{(i-1)j}v_{(i+1)j}\end{array}}{\left[(u_{(i+1)j} - u_{(i-1)j})^2 + (v_{(i+1)j} - v_{(i-1)j})^2\right]}. \quad (9)$$

The mean summary postural curvature, $\bar{\kappa}_p$, can then be calculated as follows:

$$\bar{\kappa}_p = \frac{\sum_{j=1}^{n-1}\sum_{i=1}^{29}|\kappa_{ij}|}{n}. \quad (10)$$

Note that this Equation (10) is an estimate of the average over time of the sum of the curvature on the length of the postural midline.

To determine which set of undulatory and postural reconfiguration metrics best predict the whole-body composite speed, $|\bar{v}|$, we used stepwise linear regression (mixed direction, $P > 0.15$ in and out; JMP version 8). Candidate predictor variables were the fundamental undulatory frequency, f_0', P_r, $\bar{\kappa}_p$ and the standard error and standard deviation of κ_p over the video frames.

Scaling of form reconfiguration and the postural reconfiguration during yaw turns

To place the postural reconfiguration seen in yaw turns within the larger context of this reconfiguration framework, we first compared the undulatory and postural reconfiguration of a yaw turn with that of forward translational swimming. This analysis was conducted using identical methods as described in the previous section. The study species was the leopard shark, *T. semifasciata*, and an example turn and forward translation were taken from the video data described below.

To examine the scaling of form and postural reconfiguration, we measured the body morphology of *T. semifasciata* ($n = 18$) and bending of the body during yaw turning ($n = 9$ of the 18 examined for morphology). Animals ranged three-fold in total body length, L_b, from 14.9 to 48.5 cm. For nine of

the specimens, either contact radiographs were obtained from the California Academy of Sciences Ichthyology Department or preserved specimens were obtained from the Scripps Institute of Oceanography Ichthyology Collection. Detailed descriptions of animals and of the locality of collection can be found in Appendix 1 of Porter et al. (2009). We took contact radiographs of preserved specimens on Kodak Bio-Max film using a cabinet radiograph (Hewlett Packard model Faxitron). We measured L_b and maximum lateral width of the body, W (m) from each radiograph. The W was measured immediately caudal to the pectoral fins on each individual. From preserved specimens we also measured the dorso-ventral depth of the body, D. We calculated the second moment of area as follows, assuming an elliptical shape:

$$I_b = \frac{\pi}{4}\left[\frac{D}{2}\left(\frac{W}{2}\right)^3\right]. \quad (11)$$

This procedure yields a single I_b for a tapered body. The use of one I_b obscures the order of magnitude changes in I_b that occur along the tapered body of a fish (McHenry et al. 1995). However, because W is the maximum width of the body, I_b will also be maximal and its use will place an upper limit on related estimates of the stiffness of the body. Previously, we determined that maximal I_b varies significantly among species, varies regularly with changes in body length and number of vertebrae, and is a significant predictor of the bending coefficient of the body, B_b, across five species of shark (Porter et al. 2009).

Triakis semifasciata from the Santa Monica Pier Aquarium, Santa Monica, CA were used in the yaw turning trials, and the size of the animals ranged from 25.3 to 48.5 cm L_b. Body-bending coefficient, B_b (see Equation [5]), was measured from videos of animals turning. Turning was defined as a change in heading by more than $90°$ (Kajiura et al. 2003; Porter et al. 2009). Animals were filmed in tanks where both their size and the height of the water heights were constrained to elicit tight planar turns from each individual during swimming (Porter et al. 2009). Video was analyzed at 640×480 pixels, a resolution that allowed us to see the body outline as well as the eye and dorsal fins from each individual. We determined two frames of interest from each turn: (1) the frame before initiation of a turn when the body was straight to determine body L_b and (2) the frame where the chord length, L_1, the distance between the tip of the animal's nose and the tip of the tail, was smallest.

From nine individuals, we analyzed 113 turns. Additionally, we determined L_b and W for each individual. As in the dataset for morphology we calculated I_b (m^4) by modeling each individual as an ellipse (Equation [11]). We estimated k', the structural stiffness proxy of the body, as in Equation (2).

Evolution of undulatory reconfiguration

For this article, we created a digital Tadro, a physics-based simulation of our robotic Tadro (Long et al. 2004, 2006). Both Tadro systems swim like fish with an undulatory tail in a 2D world (water surface), have a single tunicate-like eyespot sensitive to the intensity of a focal light gradient, and respond to light intensity with a proportional shift in the lateral orientation of the tail. The digital Tadros are autonomous in the sense that their behavior is not programmed; instead behavior results from the interaction of each individual Tadro with its local environment. The digital Tadros are self-propelled, with the undulatory motion of the tail prescribed by the frequency of the undulatory cycle, f, and the lateral amplitude of the undulatory motion. The propulsive wavelength, λ, of the tail is a function of the tail's structural stiffness, k_t, with λ proportional to the square root of k_t as expected by engineering theory and empirical measurements using self-propelled elastic models of fish (McHenry et al. 1995). See Appendix 1 for details of the digital Tadro model.

We created three different worlds in which to simulate the evolution of the Tadros. In World 1, k_t varied while f was held constant; in World 2, k_t was held constant while f varied; in World 3, both were allowed to vary. These three worlds allowed us to test (1) if k_t and f, by themselves, would evolve under selection for enhanced forage navigation (Worlds 1 and 2) and (2) if the two can co-exist as balanced targets of selection (World 3). Evolutionary changes in both k_t and f are related directly to undulatory reconfiguration. As k_t evolves, so too will the undulatory wavelength, λ, and hence the wave speed of the tail (see Appendices). As f evolves, so too will the wave speed, where the wave speed is the product of f and λ. Each of the 32 replications performed in each of the three worlds consisted of 25 iterations. Each iteration, in turn, consisted of 144 generations for a total of 3600 generations per replication.

We used a genetic algorithm (GA)-based optimizer that has been shown to work well for problems in high dimensional spaces (Liew 2004; Liew and Lahiri 2005). The two major issues in finding a good solution in high-dimensional spaces are (1) convergence, especially when good solutions lie in a very small region of space, and conversely (2) premature convergence where the optimizer finds solutions in a local optimum when there are better solutions in other parts of the space. We selected a GA-based optimizer because they overcome both issues in a variety of optimization problems using an iterative approach (Rasheed et al. 1997).

At the beginning of each GA iteration the optimizer evaluated a number of variable Tadros in the space and then found a good solution using a gradient descent method. Within each iteration, the optimizer created a number of generations of the population pool. In each generation, selection, mutation, and mating were used to produce one new individual from a pair of individuals in the population. The new individual was added to the population and the lowest ranked individual (using the fitness function, see Equation [12]) was removed from the population. The best individual in the population found at the end of each iteration, along with 69 new individuals selected at random, formed the initial population for the next iteration. Keeping the best individual from iteration to iteration ensured the adapted genotype would not be lost. Furthermore, when the optimizer converged on a solution, the best individual from a generation remained unchanged as the GA-created new generations.

The structure of this GA approach differs from biological evolution in that (1) individuals are added and removed from the population sequentially; (2) individuals are tested alone; and (3) the best-adapted individual is never lost. The fitness, Φ_{ij}, for any individual Tadro, i, in generation, j, was determined as follows:

$$\Phi_{ij} = \tfrac{1}{4}\left(\Delta d_{ij} + \Delta t_{ij} + \Delta U_{ij} + \Delta w_{ij}\right) \qquad (12)$$

where Δd_{ij} is the difference between the population's maximal d_j and the individual's d_i (cm), where d is the average radial distance of an individual Tadro from the light source; Δt_{ij} is the difference between the population's maximal time t_j and the individual's t_i, where t is the average time for an individual Tadro to reach a predefined area (50-cm radius) around the light source (s); ΔU_{ij} is the difference between the individual's U_i and the population's minimal U_j (cm s^{-1}), where U is the individual Tadro's average speed; and Δw_{ij} is the difference between the population's maximal w_j and the individual's w_i (radius s^{-2}), where w is the yaw wobble of an individual's body, defined as the standard

deviation of the Tadro's change in rotation rate over time. All differences are scaled by the range of values measured in that generation. Thus, Φ_{ij} attempts to select simultaneously, within a generation, for "smaller" values of d, t, and w and "larger" values of U. Please note that selection may occur by acting on only a subset of these variables, creating an evolutionary pattern, for example, where U actual decreases over time. To create an index that was not normalized to values within a generation we calculated the navigational prowess, NP, the sum of the raw values of d, t, U, and w.

Results

Undulatory and postural reconfiguration

In translationally swimming hagfish, undulatory errors, $\vec{U}_{e_i}$, show that an individual can vary from nearly pure undulatory reconfiguration (Fig. 2A) to undulatory reconfiguration with large amounts of postural reconfiguration (Fig. 2B). In those two extremes, the postural reconfiguration index, P_r, was 0.05 and 0.94 while the whole-body composite speed, $|\bar{v}|$, only varied from 16.0 to 14.5 cm s^{-1}. The reconstructed postural midlines in these two trials illustrate a pattern of little postural reconfiguration (Fig. 2C) and postural reconfiguration that varies as a standing wave at a frequency close to that of the motion of the midline of the body (Fig. 2D). The postural midline increases in curvature with the addition of a second-order secular acceleration term (Fig. 2E).

Nearly pure undulatory reconfiguration in hagfish ($P_r = 0.05$ trial) was reconstructed point-by-point with excellent fidelity by the fundamental frequency, f_0, the first harmonic, f_1, and the secular velocity in axial, v, and lateral, u, dimensions. These elements reconstructed nearly 90% of the overall motion in all points except the axial motion of the points near the head (Fig. 3A). In the lateral motion, most of the motion was reconstructed by f_0; a full wavelength was included on the body, as shown by the phase of points (magenta to magenta values). In the axial dimension, most of the motion was reconstructed by f_1; two full wavelengths were present (blue to blue to blue phase values).

In a hagfish swimming with large amounts of postural reconfiguration ($P_r = 0.94$ trial), f_0, f_1, and $\dot{u}$ reconstructed the lateral motion well but left a large gap in the axial motion, roughly mid-caudally, at 0.8 of body length (Fig. 3B). The addition of a secular acceleration term improved the fit so that >90% of the overall motion was explained in both dimensions (Fig. 3C). In other words, postural reconfiguration superimposed on undulatory reconfiguration creates a body motion in which points are accelerating constantly in different directions relative to each other, as indicated by the orientation of the triangles representing the acceleration terms (Fig. 3C).

Postural reconfiguration, measured as either P_r or summary postural curvature, $\bar{\kappa}_p$, appeared to have little influence on composite speed of the whole-body in forward-swimming hagfish or forward-swimming and backward-swimming lamprey (Fig. 4). Instead, the $|\bar{v}|$ was predicted with high fidelity by the fundamental undulation frequency of the whole-body, f'_0, in lamprey swimming forward ($r^2 = 0.69$, $P < 0.0001$, $n = 20$) and backward ($r^2 = 0.85$, $P < 0.0001$, $n = 13$), as determined by stepwise linear regression (Fig. 4A). By the same procedure, the $|\bar{v}|$ of forward swimming hagfish was predicted by f'_0 and P_r ($r^2 = 0.64$, $P < 0.0001$ for the whole multivariate regression, $n = 23$; the coefficients were $f_0 = 11.0$ with $P < 0.001$ and $P_r = -6.5$ with $P = 0.01$) (Fig. 4B).

Even though $\bar{\kappa}_p$ is not statistically linked to $|\bar{v}|$, the pattern of the two shows a clear demarcation between forward and backward swimming (Fig. 4C). Thus, while $\bar{\kappa}_p$ within a direction does not predict $|\bar{v}|$, regions of the ($|\bar{v}|$, $\bar{\kappa}_p$) plane are associated with swimming in different directions. Also, $\bar{\kappa}_p$ is correlated with P_r (Fig. 4D), as determined by linear regression in forward-swimming hagfish ($r^2 = 0.377$, $P = 0.002$, $n = 23$), forward-swimming lamprey ($r^2 = 0.310$, $P = 0.011$, $n = 20$), and backward-swimming lamprey ($r^2 = 0.761$, $P < 0.0001$, $n = 13$).

Scaling of form and postural reconfiguration in yaw turning

In terms of undulatory and postural reconfiguration in leopard sharks, turning in yaw differs dramatically from forward translational swimming (Fig. 5). During a yaw turn, the posture midline leads the reconstructed midline through the turn (Fig. 5A). Since the difference between the reconstructed midline and the posture midline represented the undulatory components of the total motion, a yaw turn shows clearly how undulatory and postural reconfiguration can be independently controlled to create a turn. In terms of harmonic structure, the yaw turn is also qualitatively different from forward translational swimming (compare Fig. 5B and C). Unlike forward translational swimming, yaw turns do not possess a wavelength, λ, in either the lateral or axial direction at any frequency that is less that the body length. In addition, yaw turns have greater magnitudes of axial motion and secular velocities.
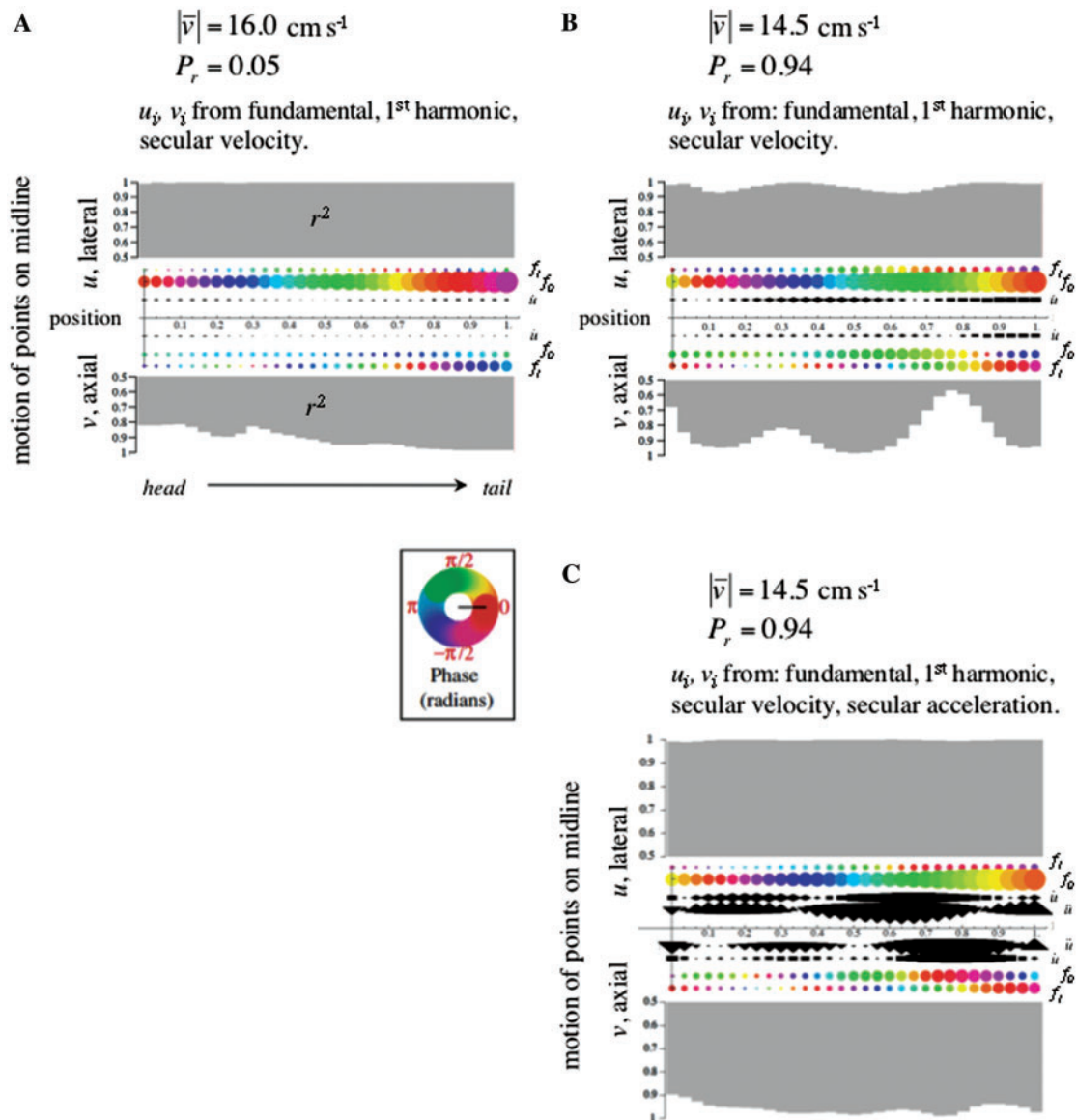
Fig. 3 Harmonic decomposition of undulatory reconfiguration more accurately represents forward translational swimming with low values of the postural reconfiguration index, P_r, compared to those with high P_r. For each of 31 points along the hagfish's dorsal midline, the lateral and axial motion over the swimming trial are reconstructed as the harmonic elements, the fundamental frequency, f_0, and its first harmonic, f_1, and a secular velocity component, $\dot{u}$ that is a deviation from the whole-body composite velocity, $|\bar{v}|$. The relationship between points is represented by their phase, which is color-coded; if different points have the same color then they are oscillating in phase in that dimension. The area of frequency and velocity points indicates relative amplitude; the shape of the velocity points indicates movement of a point forward (diamond in axial), backward (rectangle in axial), left (diamond in lateral), or right (rectangle in lateral). The goodness of fit for each point in each dimension is measured by the r^2 value as indicated by the magnitude of the gray bar in register with each point. If the r^2 value > 0.50, the bar is colored red and the right-hand y-axis should be used. The parts (A), (B), and (C) describe the postural reconstructions shown in Fig. 2 parts (C), (D), and (E), respectively. The third plot shows the second trial fit with constant secular acceleration, $\ddot{u}$, denoted by triangles. These are large, indicating that the acceleration component of the motion is significant. Note also that the r^2 values are higher, indicating an improvement in the fit, in some positions the improvement is substantial even given the additional degree of freedom at each body point and in each dimension.

The developmental scaling of leopard sharks' body form was statistically indistinguishable from linear isometry and stiffness-based allometry (Fig. 6A). The bodies' second moment of area, I_b, scaled to the 1.215 power with respect to the cube of the body length, L_b^3. The structural stiffness proxy, k', did not predict the postural reconfiguration measured by the body-bending coefficient, B_b, during
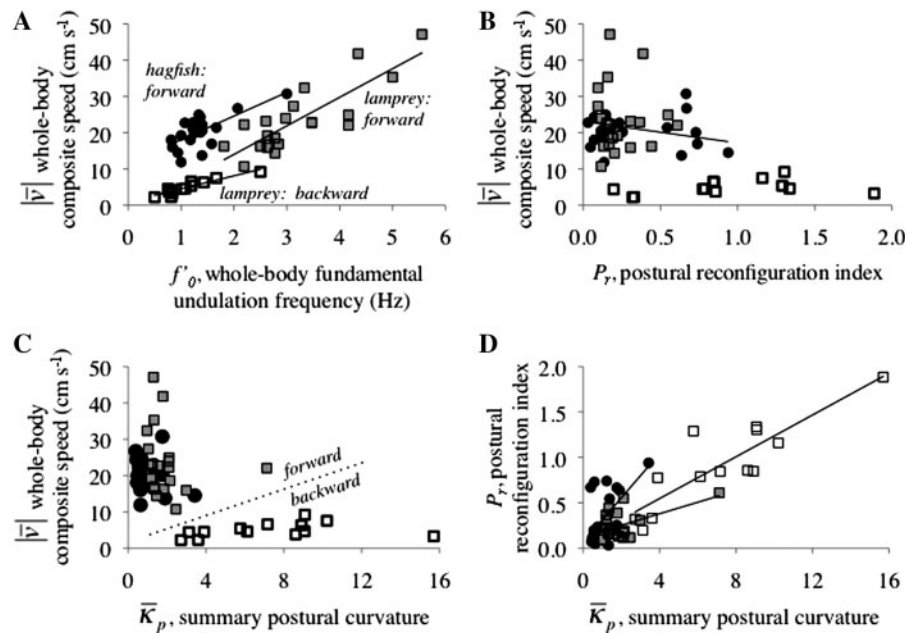
Fig. 4 Undulatory and postural reconfiguration predict translational swimming speed. (A) Whole-body composite speed, $|\bar{v}|$, is predicted by the fundamental whole-body undulation frequency alone in lamprey swimming forward ($r^2 = 0.69$; gray squares) and backward ($r^2 = 0.85$; open squares); speed is predicted, in part, by frequency in hagfish ($r^2 = 0.64$ for whole model, including P_r; black circles). (B) In hagfish but not lamprey, postural reconfiguration index predicts a portion of the variance in speed (the estimated slope of -6.5, determined by multiple regression, is shown by the line). (C) For either species or direction of swimming, speed is uncorrelated with summary postural curvature; lamprey swimming backward have higher values of summary postural curvature and lower speeds compared to the conditions when swimming forward. (D) Postural reconfiguration index and summary postural curvature are tightly correlated within species and direction. See Results section for statistics.

routine yaw turns (Fig. 6B). However, we note that k increases with increasing L_b while maximal B_b remains constant at 0.8.

Evolution of reconfiguration

Like their physically embodied robotic counterparts, digital Tadros detected, oriented to, and orbited around a light source using cycloptic helical klinotaxis (Fig. 7). Structural stiffness of the tail, k_t, and undulatory cycle frequency, f, evolved directionally over the course of the simulation under selection for enhanced forage navigation (Fig. 8). The small-scale temporal patterns of evolutionary change were realistic, with variable rates, oscillation in direction, and eventual asymptotic behavior. The asymptotic behavior in both examples (Figs. 8 and 9) was indicative of the simple global optimum found in all evolutionary trials in World 1 (k_t variable; f constant) and World 2 (k_t constant; f variable). In World 1, the initial stiffness, k_0, of the tail starts at values above and below the optimum k_t of $4.7 \, \text{mN m}^{-1}$; in all cases the optimum is achieved at rates that are variable depending on the difference between the starting value of k_t and the optimal value (Fig. 10). In World 2 the pattern is simpler

(not shown), since f_0 always had values above the f optimum of 3.4 Hz. In Worlds 1 and 2, k_t and f evolve when each is coded alone to be the variable, heritable, and evolvable trait (Fig. 11). However, when both are coded to evolve (World 3), only k_t does so (Fig. 11). Thus, k_t appeared to be the more sensitive target for selection.

It is interesting to note that while k_t is the clear target of selection throughout the simulations, based on predictable evolutionary response and positive relation to fitness (Fig. 11), the evolutionary response is mediated through the sub-behaviors (Fig. 9) that make up the fitness function (see Equation [12]). In the specific example given (Figs. 8 and 9), three of the four sub-behaviors of the population—mean distance from the light source, d, mean time to reach the light source, t, and, mean wobble of the Tadro, w—covary over time and increase fitness (recall that lower values of each are rewarded). At the same time we would expect the mean velocity, U, to increase, since higher values are rewarded by fitness; the opposite occurs in this case (Fig. 9), even though overall U is positively correlated with fitness (Fig. 11). These variable patterns demonstrate that the sub-behaviors can behave independently depending
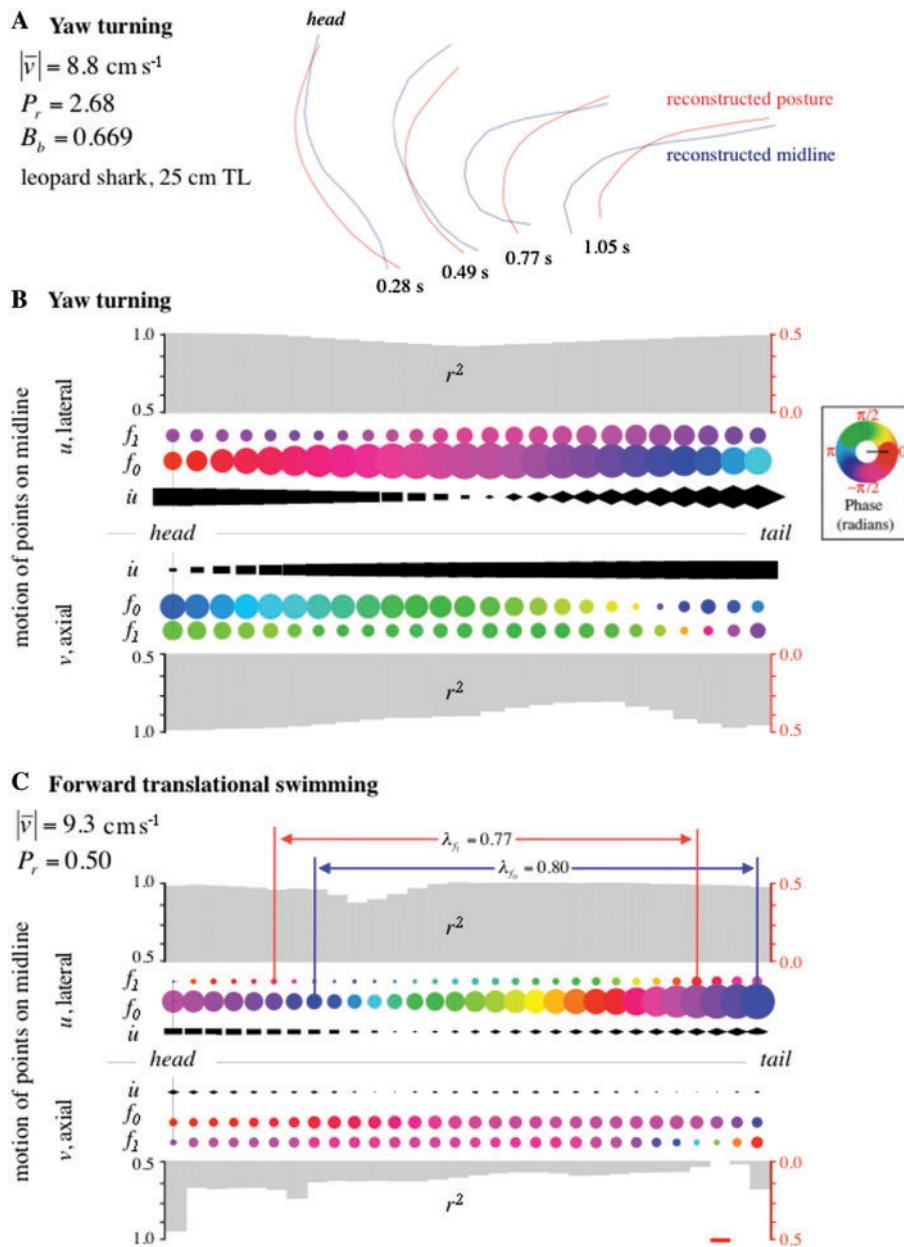
Fig. 5 Turning in the leopard shark, *T. semifasciata*, differs from forward translational swimming in terms of both undulatory and postural reconfiguration. (A) A yaw turn, as illustrated by reconstructed midlines of the body (blue) displaced laterally to show the motion at different times during the turn. The midline is reconstructed from the fundamental frequency, f_1, its first harmonic, f_0, and a secular velocity, $\dot{u}$, for each point in the axial and lateral dimension. The non-harmonic components of the motion yield the postural midline (in red), which we consider to be, over time, postural reconfiguration. The postural reconfiguration index, P_r, is greater than any P_r measured for translational swimming in lamprey and hagfish (Fig. 4). The body bending coefficient, B_b, and composite speed of the whole body, $|\bar{v}|$, are also given. (B) A yaw turn (same as in A), quantified by harmonic decomposition of the lateral and axial motion of each point. Colors, shapes, and sizes have the same meaning here as they do in Fig. 3. Note the excellent fit, as indicated by the high r^2 values. Also note that in neither dimension nor frequency is a complete wave present on the body. A yaw turn is thus characterized by (1) the presence of standing waves or traveling waves with lengths, λ, much greater than the length of the body; (2) unidirectional axial $\dot{u}$ values of high magnitude relative to the motions of the undulatory components; and (3) bidirectional lateral $\dot{u}$ values that increase in magnitude near the head and tail. (C) Forward translational motion of the same leopard shark quantified in the same fashion. Note the excellent fit, as indicated by r^2 values, of the lateral motion and the good, but not great, fit of the axial motion. For the lateral motions, a full λ is present on the body for both f_0 and f_1; the same pattern is seen in hagfish (Fig. 3). Unlike hagfish, however, the axial components in the leopard shark do not show evidence of a traveling wave of λ less than that of the body. Compared to the yaw turn (in B), forward translational swimming is characterized by (1) the presence of traveling waves in the lateral dimension with λ values less than that of the body; (2) axial and lateral $\dot{u}$ values of low magnitude relative to the motions of the undulatory components; and (3) axial motions and lateral f_1 motions of magnitude lower than that of the lateral f_0.
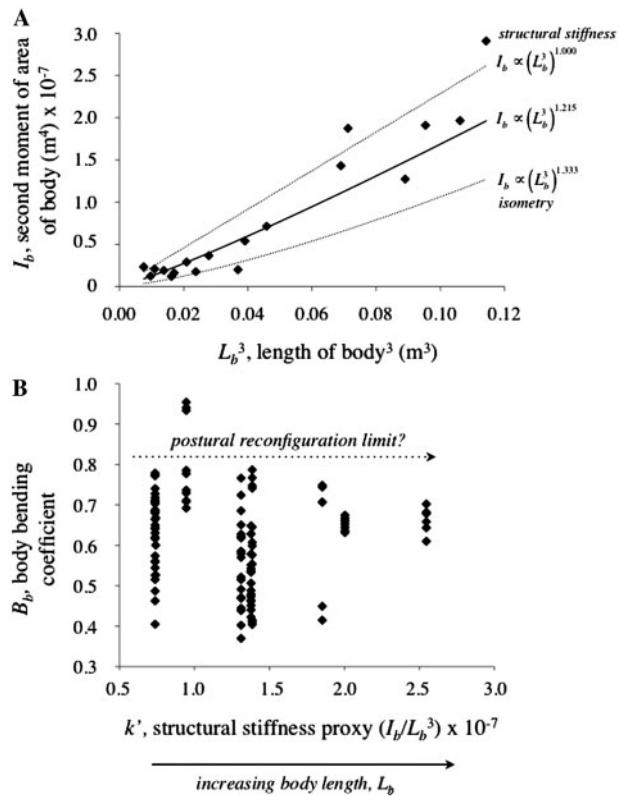
Fig. 6 Scaling of body form and postural reconfiguration in the leopard shark, *Triakis semifaciata*. (A) Scaling of form. Under isometric scaling, the second moment of area of the body, I_b (m^4) would scale with the body length cubed, L_b^3, to the 4/3 (1.333) power. Under allometric scaling governed by the mechanics of structural stiffness, I_b and L_b^3 would scale to the 1.0 power (see text for equation). In 18 individuals (black dots), the exponent of the power fit was 1.215 (solid line; $r^2 = 0.822$, $P < 0.0001$, $F = 74.022$, $n = 18$) with upper and lower 95% confidence limits, respectively, of 1.490 and 0.939; thus the data refute neither the isometric nor the allometric-spring-stiffness hypotheses. Nine individuals were measured from museum specimens; nine were measured from videos of live fish. Mean lengths of the two samples were not statistically distinguishable (*t*-test, two-tailed). (B) Scaling of postural reconfiguration. Postural reconfiguration, as measured by the body-bending coefficient, B_b, during routine yaw turns, scales in a manner that is consistent with either isometric-stiffness or allometric-stiffness scaling hypotheses. In the nine individuals measured on video, B_b did not correlate ($P > 0.05$, linear regression) with the structural stiffness proxy of the body, k', in trials with maximal B_b ($n = 9$) or all B_b trials ($n = 113$, illustrated). If these 113 points accurately sample B_b during yaw turning, then the fact that only three trials, all from the same individual, occur with values greater than 0.8 suggests that postural reconfiguration is limited. This limit may be caused by k'. Note that k' increases with increasing L_b because the I_b scales to the fourth power of length.

Fig. 7 Evolving reconfiguration in fish-like digital robots. Digital Tadros are physics-based evolutionary simulations of robotic Tadros. Lines represent paths of individual Tadros. A total of three robotic Tadros were competed in each generation. A total of 70 digital Tadros were competed in each generation, even though only three are shown here. In both systems, the Tadros navigate up a sensory gradient, towards and around a light source (yellow star) using helical klinotaxis. Note that the helical klino-taxis is not programmed into the Tadros. Rather, it is a behavior that is emergent from the interaction of each Tadro with its sensory environment, neural architecture, and motor output.

on the particular circumstances of each unique evolutionary trial. The independence of the sub-behaviors is further demonstrated by NP, the behavioral composite of the fitness sub-behaviors,
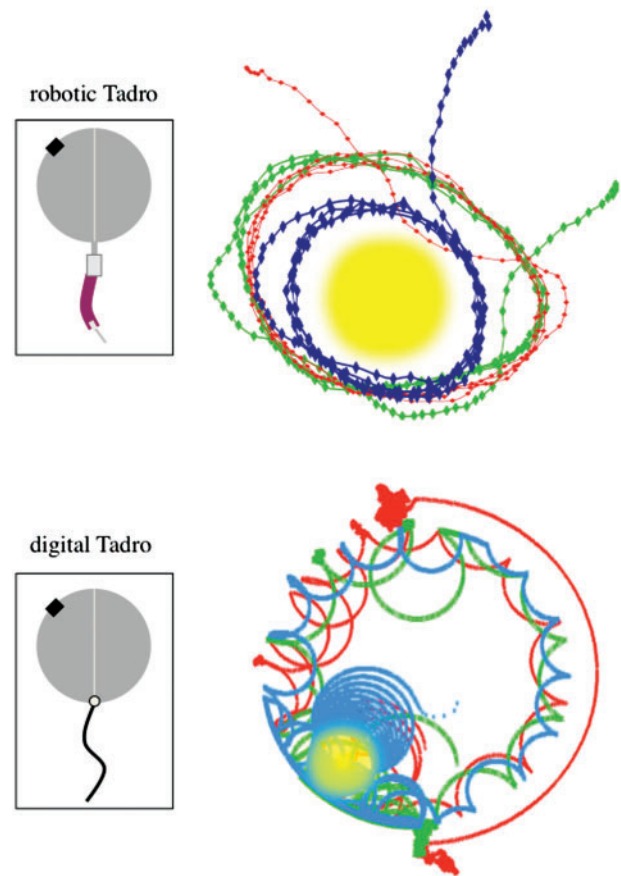
which was positively correlated with d and t in Worlds 1 and 3 and with d, t, U, and w in World 2 (Fig. 11). Overall, NP was never correlated with k_t (Fig. 11), a finding that demonstrates that it is the sub-behaviors individually and in subsets, rather than as a simple additive composite, that determine the evolution of k_t.

Discussion

Fish change their body shape in three ways that are superimposed: undulatory reconfiguration, postural reconfiguration, and form reconfiguration (Fig. 1). Undulatory reconfiguration is defined as the combined, point-by-point periodic motion of the body (Equation [8]). Deviations from undulatory
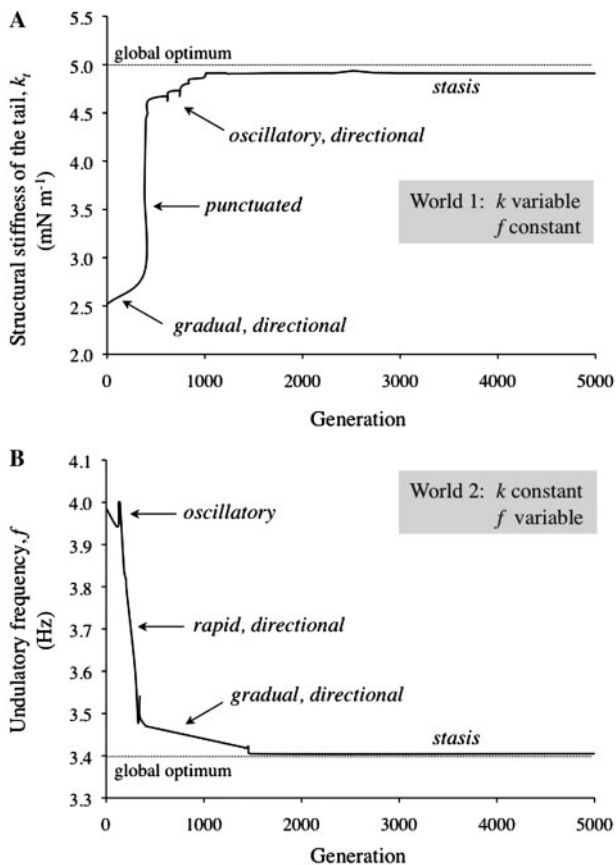
Fig. 8 Undulatory reconfiguration evolved under selection for enhanced forage navigation behavior in digital fish-like Tadros. (A) Population mean of the structural stiffness of the tail, k, is plotted over generational time. (B) Population mean of the undulatory frequency of the tail, f, is plotted over generational time. In both examples, note the realistic patterns, with different rates and local directions of evolution. These two specific examples (run 116 of World 1; run 05 of World 2) are representative of the patterns seen in all 32 trials in Worlds 1 and 2.

reconfiguration during swimming define postural reconfiguration (Figs. 2 and 3). While undulatory reconfiguration appears to be the sole or primary propulsive driver (Fig. 4A), postural reconfiguration may contribute to propulsion in hagfish (Fig. 4B) and it is associated with differences in forward swimming and backward swimming in lamprey (Fig. 4C). The modulation of the differences between undulatory reconfiguration and postural reconfiguration offers one way to understand how yaw turns are generated (Fig. 5A). Moreover, we see clear differences in the patterns of undulatory reconfiguration during yaw turning and forward translational swimming (Fig. 5B and C).

Form reconfigures over developmental time in leopard sharks in a manner that may be consistent with allometric scaling models that hold the structural stiffness of the body, k_b, constant (Fig. 6A).

However, correlation of the structural stiffness proxy, k', to body-bending coefficient, B_b, suggests an alternative: changes of k_b that occur with changes in body length may be linked to limiting maximum postural reconfiguration during routine yaw turns (Fig. 6B). When structural stiffness of the tail, k_t, in digital fish-like Tadros (Fig. 7) determines the undulating tail's propulsive wavelength it determines the tail's undulatory reconfiguration (see Appendix 1). Under selection for enhanced forage-navigation behavior, k_t evolves rapidly to a global optimum (Figs. 8 and 9). When both k_t and f are variable and heritable, k_t alone evolves (Fig. 11), even though f evolves when k_t is held constant (Figs. 8 and 11), a result that underscores the importance of k_t in modulating undulatory reconfiguration.

Modulation of swimming performance and behavior

Perhaps the most important physiological result from this study is that undulatory and postural reconfiguration can be superimposed and independently controlled (Fig. 4). Undulatory reconfiguration alone has multiple kinematic degrees of freedom (Equation [8]; Fig. 3): (1) whole-body fundamental undulation frequency, f_0; (2) whole-body first-harmonic undulation frequency, f_1; (3) phase among points in the lateral dimension; (4) phase among points in the axial dimension; (5) lateral-to-axial phase; (6) amplitude of the lateral motion; and (7) amplitude of the axial motion. Postural reconfiguration, too, has multiple kinematic degrees of freedom (Equations [8–10]; Fig. 3): (1) secular velocity at any point of the body; (2) correlated secular velocity of multiple points; (3) secular acceleration at any point of the body; (4) correlated secular acceleration of multiple points; (5) spatial pattern of magnitude of curvature along the body; (6) temporal pattern of magnitude of curvature at a given point; and (7) temporal pattern of curvature along the body. If all of these degrees of freedom were independent, an extremely large number of motions would be possible. Since fish appear to have a restricted set of motions, even in hagfish and lamprey that retain a flexible notochord as adults, we must identify which combinations are seen in live fish, under as wide a range of behavioral circumstances as possible, and what the mechanisms are of neuromuscular control.

One reason for the explosion of kinematic degrees of freedom is that our method explicitly includes axial motions and postural curvatures as putatively independent parameters. Thus, we have put a quantitative face on the well-worn caution: studies that
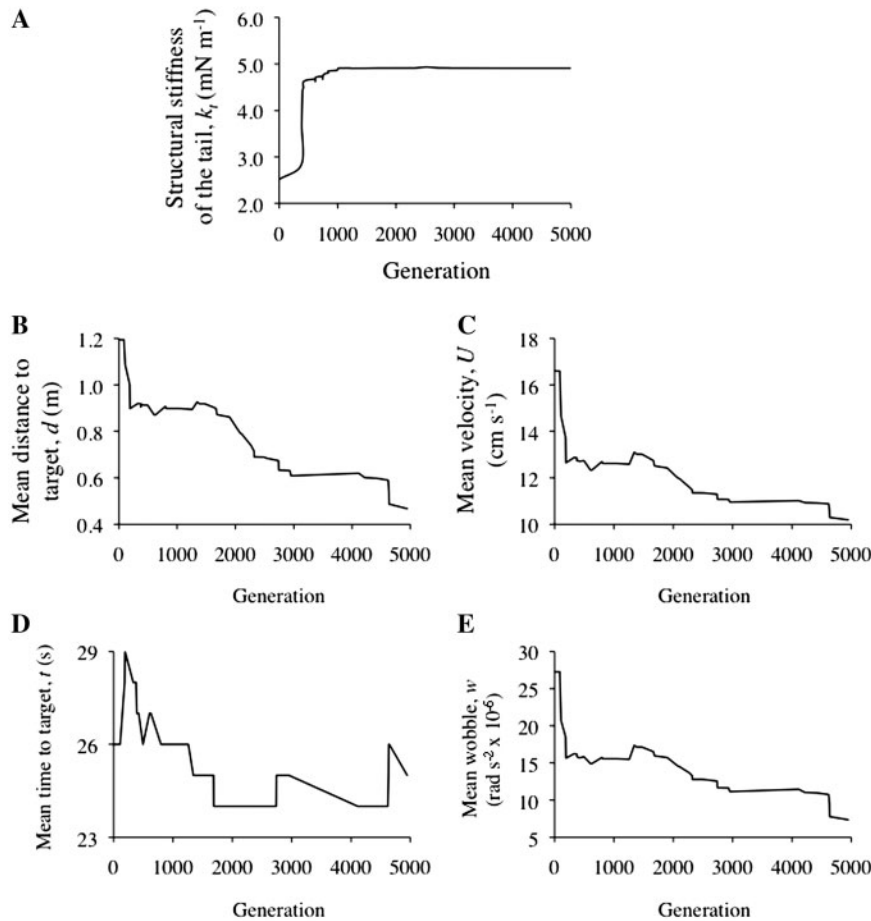
Fig. 9 Evolution of structural stiffness of the undulatory tail, k_t, in a population of digital Tadros. Specific sub-behaviors in the fitness function (see Equation [12]) varied with respect to changes in k_t in the digital Tadro populations. (A) Evolution of structural stiffness of the tail, k_t, of a population in World 1, where undulatory frequency, f, was held constant (same trials as shown in Fig. 8A). (B) Mean distance to the target, d, dropped rapidly during the time when k_t was increasing gradually and then remained stable when k_t increased in a punctuated manner at generation 380. (C) Mean velocity, U, dropped rapidly in concert with d and w as k_t increased gradually; changes in U were uncorrelated with the punctuated change in k_t. Because the sub-behaviors are free to vary independently of each other, the negative fitness effects of a decrease in U can be offset by increases in the other sub-behaviors. (D) Mean time to target, t, increased initially, in opposition to d, U, and w while k_t was increasing gradually; t dropped rapidly and in concert with punctuated changes in k_t at 380 generations. (E) Mean wobble, w, showed a pattern nearly identical to that of d and U.

restrict themselves to examining only the special cases of steady translational swimming or maximal escape responses avoid the complexities of intermediate behaviors. (We are guilty of this ourselves.)

These kinematically messy intermediate behaviors are likely what fish use when they are not in an experimental chamber. For example, in the free-swimming hagfish examined in this study, we found a statistically significant link, albeit weak (see Results section for statistics), between the postural reconfiguration index, P_r, and the whole-body composite speed, $|\bar{v}|$. Forwardly swimming hagfish reduce their P_r as $|\bar{v}|$ increases (Fig. 4B). Given that P_r is positively correlated with summary postural curvature (Fig. 4D), hagfish appear to be straightening their postural midline as they swim at faster speeds. This finding is consistent

with, and elaborates upon, a preliminary analysis of a single body point in hagfish, at which mid-line curvature was positively correlated with the angle of pitch of the tail (Long et al. 2002b).

Additional evidence for the independent control of undulatory and postural reconfiguration comes from comparing the forward- and backward-swimming of lamprey. Looking at f_0 as a predictor of $|\bar{v}|$ (Fig. 4A), the slopes for the two directions are similar and the range of points in both dimensions are nearly non-overlapping. These observations tempt one to interpret that f_0 alone distinguishes forward-swimming from backward-swimming. Instead, the postural summary curvature, $\bar{\kappa}_p$, clearly delineates the two behaviors, with backward-swimming occurring only at low magnitudes of $|\bar{v}|$ accompanied by a
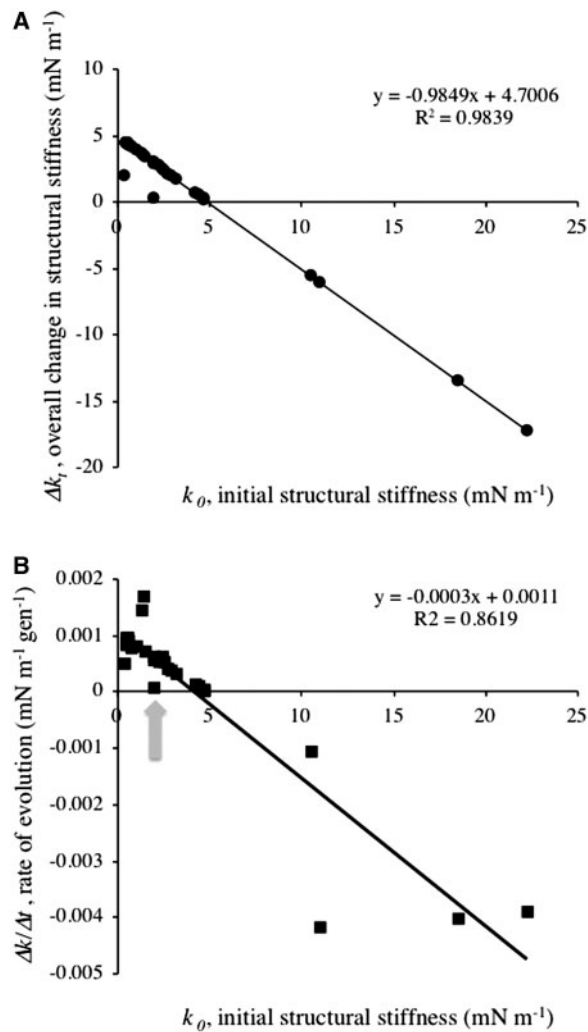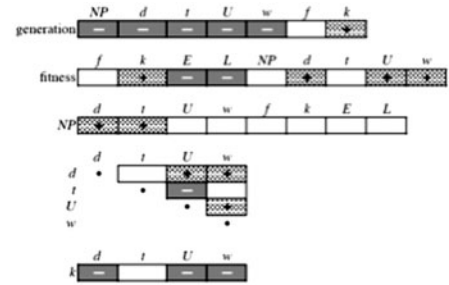
Fig. 10 Evolutionary dynamics of structural stiffness of the tail, k_t, >5000 generations in 32 populations of 70 digital Tadros under selection for enhanced forage navigation (World 1, with constant undulatory frequency, f). (A) The overall change in k_t was a function of the initial structural stiffness, k_0. The x-intercept at 5 indicates that on average this world, where k_t was variable and frequency was constant, had a single global optimum for k_t that was independent of the magnitude and direction of k_0. (B) The overall rate of evolution was also a function of k_0, suggesting that the selection gradient was similar everywhere in the fitness landscape. The arrow indicates the run examined in Figs. 8 and 9.

Fig. 11 Reconfiguration evolved in digital Tadros. Patterns of correlations for the three different worlds. In Worlds 1 and 3, structural stiffness of the tail, k_t, increased over generational time. Only in World 2, when k_t was held constant, did undulatory frequency, f, evolve. When both k_t and f can evolve, as in World 3, only k_t did. In spite of the differences in absolute magnitude (Fig. 9) of the fitness sub-behaviors d, distance to target, t, time to target, U, average swimming speed, and w, yaw wobble, they all are all correlated with fitness with the exception of t in World 3. Changes in navigational prowess, NP, the behavioral composite of the fitness sub-behaviors, were primarily correlated with d and t; NP was never correlated with k_t, but it was correlated with f in World 2. Fitness sub-behaviors were positively correlated in World 2; in Worlds 1 and 3 the pattern varied, with d positively correlated with U and w, and w positively correlated with U.

wide range of $\bar{\kappa}_p$, in general larger than those seen in forward-swimming. Thus, modulation of different swimming behaviors appears, in this case, to be enacted largely by postural reconfiguration.
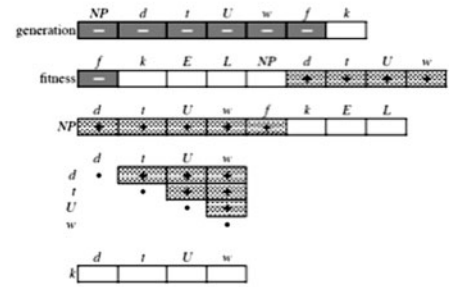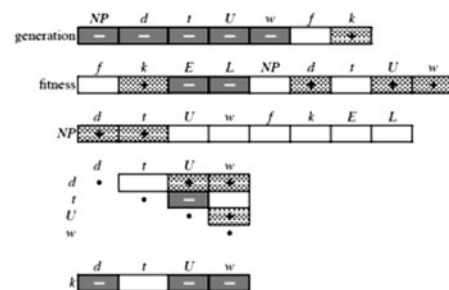
Reconfiguration of form, posture, and undulation and the structural stiffness of the body

As mentioned in the Introduction section, many lines of evidence support the hypothesis that k_b, at least in part, determines undulatory and postural reconfiguration. However, a hypothesis is only as good as its explanatory and predictive power. In this study, we tested the prediction that form should scale allometrically in order to hold k_b constant. While the data from leopard sharks failed to refute or support this prediction (Fig. 6A), or distinguish it from the prediction based on isometry, we were surprised that the k_b-hypothesis still stands, given the crude model of k_b (Equation [1]),

an over-simplified form-based proxy of structural stiffness, k' (Equation [2]), the assumption of constant Young's modulus, E, and the expectation that k_b would stay constant as body length, L_b, increased.

Contrary to the assumption of our allometric-stiffness scaling model, k' was not constant with increasing L_b but increased (Fig. 6B). With this in mind, we found the relationship between k' and B_b intriguing: an apparent upper limit for B_b of 0.8 suggests that the higher magnitudes of k' with increasing L_b may compensate for the higher bending torques expected with increasing size (M. E. Porter et al., unpublished data). To test this hypothesis, we would need to measure the Young's modulus, E, of the muscularly activated body during turns. We would predict that E, along with k', would increase or remain constant with increasing L_b.

Structural stiffness of the tail, k_t, evolved when selection enhanced forage-navigation behavior (Figs. 8A, 9 and 10). The populations of Tadros in World 1 were seeded randomly with variation in k_t, and the fitness function (Equation [12]) ranked, within a generation, individual performance in locating, orienting to, and orbiting at or near, a light source (Fig. 7B). The changes in k_t corresponded to a drop in the mean time to target, t (Fig. 9D), and not, surprisingly, to changes in the mean velocity, U (Fig. 9C). The changes in k_t were also independent of the NP the summation of the four variables used in the composite fitness function (Equation [12]): average distance of the Tadro from the light source, d, average time it took a Tadro to reach the light, t, average speed of the Tadro, U, and the average wobble of the Tadro, w (Fig. 11). By Lighthill's large-amplitude hydrodynamic theory (Lighthill 1960, 1975), k_t in the tails of digital Tadros was modeled to be proportional to the undulatory wavelength (see Appendices 1 and 2). Our results demonstrate a complex connection between evolution, behavior, undulatory reconfiguration, and k_t (Fig. 9). While our data do not elucidate the causal connections, we suspect that stiffer tails may enhance either maneuverability, by acting as a better turning rudder, or top speeds, without shifting mean velocity, because of the greater propulsive wavelengths. What is clear, however, is that k_t modulates the forage navigation behavior of digital, fish-like Tadros.

Further evidence that k_t is an important modulator of undulatory reconfiguration comes from results in Tadro World 3, when both k_t and f are variable, heritable, and can evolve (Fig. 11). In these circumstances, only k_t evolves. Thus, when selection acts on

behavior, k_t appears to be the more sensitive target for selection. Based on these simulation results, we predict that, in real fish, we would see more evolution of mechanism and structures involved in stiffness than mechanisms and structures involved in controlling f.

Into the wild

In addition to the specific results mentioned above, the approaches developed in this article present exciting opportunities for future research. First, our analysis of locomotion involves the simultaneous quantitative description of the user-defined points on the body. In the case of translational undulatory swimming, this combined analysis seeks to redefine two fundamental parameters of undulatory locomotion: (1) tail-beat frequency becomes whole-body fundamental frequency; and (2) swimming speed becomes whole-body composite speed. Because both of these parameters capture the behavior of the entire body, they are more representative of the physics of locomotion; under some conditions, e.g., the motion of the tip of the tail can differ dramatically from that of the body (Fig. 2B). When that happens, examining the frequency of the tip of the tail alone conflates undulatory and postural reconfiguration.

Second, the general methodology presented here can be applied to any animal that reconfigures—changes its body shape—in order to move and behave. Axial undulators, such as worms, snakes, and alligators, are obvious candidates. Less obvious candidates are the animals that swim, run, swing, or fly using appendages. Each appendage reconfigures during locomotion and during other behaviors that involve movement. Which, if any, of those movements involve undulatory motion? Or do appendages operate solely by means of postural reconfiguration?

Third, we are in a position to quantify undulatory and postural reconfiguration in the wild. We have shown that a single tail-beat from a swimming fish is sufficient for analysis and that investigators can measure cycle-to-cycle and behavioral differences in the proportion of undulatory and postural reconfiguration. In the wild, we can address the following questions. How often do fish vary the magnitudes and phases of superimposed undulatory and postural reconfigurations? Are maneuvers possible without postural reconfiguration? Does the relative amount of postural reconfiguration used routinely vary with life-history stage? How general are the phenomena that we see in the species studied in this article? Do bony fishes show the same kinds of kinematic and physiological behavior? Does body form scale

with regard to apparent structural stiffness of the body? Since we have shown that undulatory and postural reconfiguration can be independently controlled by fish in the laboratory, this opens up possibilities for understanding the motor and neural underpinnings of behavioral complexity under natural conditions (see also Webb 1984, 1988, 2006).

Acknowledgments

Funding

References

Doorly N, et al. 2009. Biomimetic evolutionary analysis: robotically-simulated vertebrates in a predator-prey ecology. Proceedings of the 2009 IEEE Symposium on Artificial Life. Red Hook (NY): IEEE (Curran Associates). p. 147–54.

Eaton RC, Lee RKK, Foreman MB. 2001. The Mauthner cell and other identified neurons of the brainstem escape response network. Prog Neurobiol 63:467–85.

Hale ME, Long JH Jr, McHenry MJ, Westneat MW. 2002. Evolution of behavior and neural control of the fast-start escape response. Evolution 56:993–1007.

Jayne BC, Lauder GV. 1993. Red and white muscle activity and kinematics of the escape response of the bluegill sunfish during swimming. J Comp Physiol A 173:495–508.

Kajiura SM, Forni JB, Summers AP. 2003. Maneuvering in juvenile carcharhinid and sphyrnid sharks: the role of the hammerhead shark cephalofoil. Zoology 106:19–28.

Liew CW. 2004. Using a genetic algorithm to optimize the gape of a snake jaw. Proceedings of the Twenty Fourth ACM Symposium on Applied Computing. New York: Association for Computing Machinery. p. 975–9.

Liew CW, Lahiri M. 2005. Exploration of convergence? Another metacontrol mechanism for gas. Proceedings of Eighteenth International Florida AI Research Society Conference. Menlo Park (CA): American Association for Artificial Intelligence Press. p. 251–7.

Lighthill MJ. 1960. Note on the swimming of slender fish. J Fluid Mech 9:305–17.

Lighthill MJ. 1975. Mathematical biofluiddynamics. Philadelphia: Society for Industrial and Applied Mathematics.

Long JH Jr. 1995. Morphology, mechanics, and locomotion: the relation between the notochord and swimming motions in sturgeon. Environ Biol Fishes 44:199–211.

Long JH Jr, Nipper KS. 1996. The importance of body stiffness in undulatory propulsion. Am Zool 36:678–94.

Long JH Jr, Hale ME, McHenry MJ, Westneat MW. 1996. Functions of fish skin: flexural stiffness and steady swimming of longnose gar, *Lepisosteus osseus*. J Exp Biol 199:2139–51.

Long JH Jr. 1998. Muscles, elastic energy, and the dynamics of body stiffness in swimming eels. Am Zool 38:771–92.

Long JH Jr, Adcock B, Root RG. 2002a. Force transmission via axial tendons in undulating fish: a dynamic analysis. Comp Biochem Physiol A 133:911–29.

Long JH Jr, Koob-Emunds M, Sinwell B, Koob TJ. 2002b. The notochord of hagfish, *Myxine glutinosa*: viscoelastic properties and mechanical functions during steady swimming. J Exp Biol 205:3819–31.

Long JH Jr, Lammert AC, Pell CA, Kemp M, Strother J, Crenshaw HC, McHenry MJ. 2004. A navigational primitive: biorobotic implementation of cycloptic helical klinotaxis in planar motion. IEEE J Oceanic Eng 29:795–806.

Long JH Jr, Koob TJ, Irving K, Combie K, Engel V, Livingston N, Lammert A, Schumacher J. 2006. Biomimetic evolutionary analysis: testing the adaptive value of vertebrate tail stiffness in autonomous swimming robots. J Exp Biol 209:4732–46.

McHenry MJ, Pell CA, Long JH Jr. 1995. Mechanical control of swimming speed: stiffness and axial wave form in an undulatory fish model. J Exp Biol 198:2293–05.

Porter ME, Roque CM, Long JH Jr. 2009. Turning maneuvers in sharks: predicting body curvature from body and vertebral morphology. J Morph 270:954–65.

Rasheed K, Hirsh H, Gelsey A. 1997. A genetic algorithm for continuous design space search. Artif Intell Eng 11:295–305.

Root RG, Courtland H-W, Pell CA, Hobson B, Twohig EJ, Suter RJ, Shepherd WR III, Boetticher N, Long JH Jr. 1999.

Swimming fish and fish-like models: the harmonic structure of undulatory waves suggests that fish actively tune their bodies. Proceedings of the 11th International Symposium on Unmanned Untethered Submersible Technology (UUST). Lee (NH): Autonomous Undersea Systems Institute. p. 378–88.

Root RG, Courtland H-W, Shepherd W, Long JH Jr. 2007. Flapping flexible fish: periodic and secular body reconfigurations in swimming lamprey, *Petromyzon marinus*. Exp Fluids 43:779–97.

Webb PW. 1984. Body form, locomotion and foraging in aquatic vertebrates. Am Zool 24:107–20.

Webb PW. 1988. Simple physical principles and aquatic vertebrate locomotion. Am Zool 28:709–25.

Webb PW. 2006. Stability and maneuverability. In: Shadwick RE, Lauder GV, editors. Fish physiology. San Diego: Elsevier Press. p. 281–332.

Westneat MW, Hale ME, McHenry MJ, Long JH Jr. 1998. Mechanics of the fast-start: Muscle function and the role of intramuscular pressure in the escape behavior of *Amia calva* and *Polypterus palmas*. J Exp Biol 201:3041–55.

Appendix 1

Digital Tadro model

We modeled the digital Tadro with the following assumptions. The basin of the robot is reduced to a disc with a keel, and the tail to a line segment that extends from the posterior of the body (Fig. 6). We used Lighthill's slender-body theory (Lighthill 1960, 1975) to calculate the thrust and drag generated as the digital Tadro swims. The model tracks position on the surface of a 2D tank which extends infinitely in each direction. A single source of light is at a fixed height above the pool, adding a third dimension.

Each Tadro's location and velocity in absolute coordinates are unknowns described by the model. The location is given by $x(t) = (x(t), y(t))$ with initial values $x(0) = x_0 = (x_0, y_0)$, velocity $x' = v = (u, v)$, $v(0) = v_0 = (u_0, v_0)$, and acceleration $x'' = a$. The governing parameters for the model are: (1) M, mass of the Tadro; (2) moi, mass moment of inertia of the Tadro; (3) R, radius of the Tadro body; (4) L_D, depth of the Tadro body underwater; (5) L_T, length of the Tadro's tail; (6) A_T, area of the lateral face of the tail; (7) D_K, depth of the keel; (8) A_K, area of the lateral face of the keel (for a rectangular keel, $A_K = 2RD_K$); (9) $F^2 = EI/\rho\tau$ ratio of flexural stiffness to mass density (per unit length) of tail, (1) f, undulatory frequency of the tail. In addition, the mass density of water was set, $\rho_{water} \approx 1000\,\mathrm{kg\,m^{-3}}$, and the Reynolds number was $Re \approx 10^5$. The initial conditions x_0, y_0, θ_0, v_0, u_0, and ω_0 are also parameters in the model.

In order to solve the system numerically, we expressed it in a system of six equations in the six scalar unknowns: x, y, θ, v, u, and ω. The first three equations are the definitions:

$$\dot{x} = u \tag{1}$$

$$\dot{y} = v \tag{2}$$

$$\dot{\theta} = \omega \tag{3}$$

Then:

$$
\begin{aligned}
\dot{u} = \frac{1}{M}\Bigg\{ &T\cos\phi - C_{D1}RL_D Vu - \frac{A_T}{16}C_N(\gamma) \\
&\times [(4v - L_T\omega\cos\phi - 4R\omega\cos\phi - L_T\omega\cos(\beta+\phi)) \\
&\times (2v\cos\phi - 2u\sin\phi - 2R\omega - L_T\omega\cos\beta) \\
&- 4(u\cos\phi + v\sin\phi)(2u + \omega(2R + L_T\cos\beta)\sin\phi)] \\
&+ \frac{A_K}{2}C_N(\gamma')[(v^2 - u^2)\cos\theta - 2uv\sin\theta]\Bigg\}
\end{aligned}
\tag{4}
$$

$$
\begin{aligned}
\dot{v} = \frac{1}{M}\Bigg\{ &T\sin\phi - C_{D1}RL_D Vv - \frac{A_T}{16}C_N(\gamma) \\
&\times [(4u - L_T\omega\sin\theta - 4R\omega\sin\phi - L_T\omega\sin(\beta+\phi)) \\
&\times (2u\sin\phi - 2v\cos\phi + 2R\omega + L_T\omega\cos\beta) \\
&- 4(u\cos\phi + v\sin\phi)(2v - \omega(2R + L_T\cos\beta)\cos\phi)] \\
&+ \frac{A_K}{2}C_N(\gamma')[-2uv\cos\theta + (v^2 - u^2)\sin\theta]\Bigg\}
\end{aligned}
\tag{5}
$$

$$
\begin{aligned}
\dot{\omega} = \frac{1}{\mathrm{moi}}\Bigg\{ &-TR\sin\beta - 0.006\pi R^4(L_D + \tfrac{1}{4})|\omega|\omega \\
&- \frac{A_T C_N(\gamma)}{16\sqrt{2}V}(2R + L_T\cos\beta) \\
&\times [\omega(2R + L_T\cos\beta)(u\cos\theta + v\sin\theta) + 2V^2\sin\beta] \\
&\times [8V^2 + (2L_T^2\cos^2\beta + 8L_T R\cos\beta + 8R^2)\omega^2 \\
&+ 4L_T[u(\sin\theta + \sin(2\beta+\theta)) \\
&+ v(\cos\theta + \cos(2\beta+\theta))] + 16R(u\sin(\beta+\theta) \\
&- v\cos(\beta+\theta))w]^{1/2} + \frac{0.007D_K}{8} \\
&\times [R^4\omega^2 + 4R^2\omega(u\sin\theta - v\cos\theta) + 4V^2]\Bigg\}
\end{aligned}
\tag{6}
$$

where $V = \sqrt{u^2 + v^2}$ $\phi = \theta + \beta$ and

$$
\begin{aligned}
T = \frac{L^2\beta}{32}[J_1(4\beta) - 4J_2(4\beta)] - \frac{V^2}{4}[1 + J_0(2\beta)] \\
- \frac{VL\beta}{4}[J_1(\beta) + J_1(3\beta)] + \frac{3L^2\beta^2}{16}
\end{aligned}
\tag{7}
$$

and where J_i is the Bessel function of the first kind with index i. The function $C_N(\gamma)$ can be expressed in terms of the parameters and variables of the problem as

$$C_N(\gamma) = \left| \frac{2\pi \left(v \cos\phi - u\sin\phi - R\omega - \frac{1}{2}L_T \omega \cos\beta \right)}{u\cos\phi + v\sin\phi} \right| \quad (8)$$

if

$$\left| 2\pi \left(v\cos\phi - u\sin\phi - R\omega - \tfrac{1}{2}L_T\omega\cos\beta \right) \right| < V\sin\tfrac{\pi}{18} \quad (9)$$

and

$$C_N(\gamma) = \left(0.222 + 0.283 \frac{V}{\left| v\cos\phi - u\sin\phi - R\omega - \frac{1}{2}L_T\omega\cos\beta \right|} \right)^{-1}. \quad (10)$$

In a similar fashion, we can express $C_N(\gamma')$ as

$$C_N(\gamma') = \left| \frac{2\pi(u\cos\theta + v\sin\theta)}{v\cos\theta - u\sin\theta} \right| \quad (11)$$

if

$$|u\cos\theta + v\sin\theta| < V\sin\tfrac{\pi}{18} \quad (12)$$

$$C_N(\gamma') = \left(0.222 + 0.283 \frac{V}{|u\cos\theta + v\sin\theta|} \right)^{-1}. \quad (13)$$

The evolution of the digital Tadro was treated as an optimization problem with the following seven variables: (1) EI, flexural stiffness of the tail; and (2) L_T, length of the tail, combine (see Equation [1] in the Introduction section) to form the structural stiffness of the tail, k; (3) f, undulatory frequency; and the four initial conditions (4) speed in the x direction; (5) speed in the y direction; (6) angular velocity; and (7) orientation of the Tadro.

While we have attempted to model the robotic Tadros (Long et al. 2006), some important discrepancies exist between robotic and digital forms:

(1) Speed: the robotic Tadros begin at rest, and pick up speed as they swim, obtaining a mean speed of $0.069 \pm 0.0014\,\mathrm{m\,s^{-1}}$. The digital Tadros must begin with an initial speed of at least $0.3\,\mathrm{m\,s^{-1}}$ (due to limitations of the Lighthill model) and remain above this speed throughout.

(2) Fluid forces: the digital Tadros experience a simplified flow regime in which the net force acting on the Tadro is the sum of the thrust from the tail and drag and lift acting on the body. Unsteady forces are omitted and would be present in the physically embodied Tadros.

(3) Tank dimensions: the robotic Tadros swim in a tank 3 m in diameter, whereas the digital Tadros swim in a tank of infinite size. Thus, interactions with walls are not modeled here.

(4) Tadro interactions: three robotic Tadros competed simultaneously, allowing for physical interactions among them. The digital Tadros complete the navigation task one at a time.

Appendix 2

List of variables used in text (not included those used in Appendix 1).

Variable	Name	Units	Equation in which the variable is first used
a_f	Amplitude of the fundamental frequency	cm	8
a_1	Amplitude of the first harmonic frequency	cm	8
B_b	Body-bending coefficient	–	5
d	Average radial distance of a Tadro from a light source	cm	–
Δd_{ij}	Difference between the population's maximal d and the individual's d	cm	12
D	Dorso-ventral depth of the body	m	11
E_b	Apparent Young's modulus of the body	Pa	1
f	Frequency of the undulatory cycle	Hz	–
f'_0	Fundamental undulatory frequency of the whole body	Hz	–
i	Index for points on the body; index for individual Tadro	–	6; 12
I_b	Second moment of area of the body	m^4	1
j	Index for video frame; index for generation	–	9; 12
k_b	Structural stiffness of the body	$N\,m^{-1}$	1
k_t	Structural stiffness of the tail	$N\,m^{-1}$	–
k_0	Initial structural structure stiffness of the tail	$N\,m^{-1}$	–
k'	Structural stiffness proxy	m	2
L_b	Total length of the body	m	1
L_l	Chord length from tip of the rostrum to the tip of the tail	m	5
n	Number of full-cycle analysis windows	–	7
NP	Navigational prowess	–	–
P_r	Postural reconfiguration index	–	7
t	Time or mean time for a Tadro to reach the light source	s	8; –
Δt_{ij}	Difference between the population's maximal t and the individual's t	s	12
u	Axial motion of a point on the body	cm	8
$\dot{u}$	Axial, secular velocity of a point on the body	$cm\,s^{-1}$	8
$\ddot{u}$	Axial, secular acceleration of a point on the body	$cm\,s^{-2}$	8
U	Average speed of a Tadro	$cm\,s^{-1}$	–
ΔU_{ij}	Difference between the individual's U and the population's maximal U	$cm\,s^{-1}$	12
$\vec{U}_{e_i}$	Undulation error	–	6
v_i	Velocity vector of point i on the body	$cm\,s^{-1}$	6
$\bar{v}$	Average velocity vector of all points on the body	$cm\,s^{-1}$	6
$|\bar{v}|$	Composite speed of the whole body	$cm\,s^{-1}$	6
w	Wobble of the Tadro in yaw	$Radius\,s^{-2}$	–
Δw_{ij}	Difference between the population's maximal w and the individual's w	$Radius\,s^{-2}$	12
W	Maximum lateral width of the body	m	11
ϕ_f	Phase lag for the fundamental frequency	Radius	8
ϕ_1	Phase lag for the first harmonic frequency	Radius	8
Φ	Fitness of an individual Tadro	–	12
κ	Curvature of the postural midline	m^{-1}	9
$\bar{\kappa}_p$	Mean summary postural curvature	m^{-1}	10
λ	Propulsive wavelength of the tail	m	
ω	Fundamental angular frequency	$Radius\,s^{-1}$	8